SCIEPublish

Article

Effect of Magnesium Aluminum Silicate Addition on the Ablation Resistance of BN Matrix Ceramics

Delong Cai [1], Bo Wang [2,*], Haoyi Wang [2], Bo Niu [2], Xingqi Liao [2], Yanlin Dai [3], Xuan Wang [4], Zhihua Yang [2], Xiaoming Duan [2], Dechang Jia [2,*] and Yu Zhou [2,5]

[1] International Joint Laboratory of Advanced Nanomaterials of Heilongjiang Province, College of Materials Science and Chemical Engineering, Harbin Engineering University, 145 Nantong Street, Harbin 150001, China; dlcai@hit.edu.cn (D.C.)

[2] Key Laboratory of Advanced Structural-Functional Integration Materials, School of Materials Science and Engineering, Harbin Institute of Technology, Harbin 150001, China; wanghaoyiwhy@126.com (H.W.); niubo@ecust.edu.cn (B.N.); hitlxq@163.com (X.L.); zhyang@hit.edu.cn (Z.Y.); dxmhit@126.com (X.D.); zhouyu@hit.edu.cn (Y.Z.)

[3] Chongqing Changjiang Electrical Appliances Industries (Group) Co., Ltd, Chongqing 401336, China; 122037532@qq.com (Y.D.)

[4] The Fourth System Design Department, Fourth Academy, China Aerospace Science and Industry Corporation Limited, Beijing 100048, China; 86092573@qq.com (X.W.)

[5] School of Materials Science and Engineering, Harbin Institute of Technology (Shenzhen), Shenzhen 518055, China

* Corresponding author. E-mail: bowang6600@126.com (B.W.); dcjia@hit.edu.cn (D.J.)

Received: 11 May 2024; Accepted: 23 December 2024; Available online: 27 December 2024

ABSTRACT: Ablation resistance is a critical factor in evaluating the performance of BN-based ceramic composites under extreme service conditions. This study investigates the ablation behavior and underlying mechanisms of BN-MAS wave-transparent ceramic composites with varying magnesium aluminum silicate (MAS) content through oxyacetylene torch tests. The results reveal that increasing the MAS content reduces the mass ablation rate from 0.0298 g/s to 0.0176 g/s and the linear ablation rate from 0.149 mm/s to 0.112 mm/s. The incorporation of MAS into *h*-BN ceramics significantly lowers the surface ablation temperature, primarily due to the evaporation of B_2O_3 (*g*) and MAS ceramics. Cross-sectional analysis of the ablated composites indicates the presence of micro- and macro-spallation in the ablation center. The primary ablation products are magnesium-aluminum borosilicate glass and mullite. Key ablation mechanisms include the oxidation of *h*-BN under flame exposure, the erosion of viscous oxidation products, and the physical degradation of the matrix caused by the high-velocity gas flow.

Keywords: Ablation behavior; High temperature applications; Microstructure; Service reliability

1. Introduction

The radome on a high-speed vehicle is a key structural component to ensure high-precision sudden defense guidance and highly stable flight. The rapid increase of flight Mach number has put more stringent requirements on the usage performance of materials for radomes [1–4].

Hexagonal boron nitride (*h*-BN) exhibits exceptional high-temperature performance, making it a valuable material for various extreme-environment applications. It has a low density (2.27 g/cm^3) and excellent thermal stability, with no melting point and a sublimation temperature approaching 3000 °C under nitrogen or inert gas. Unlike graphite, *h*-BN does not soften under high-temperature conditions without load and demonstrates high chemical stability, offering strong corrosion resistance to acids, alkalis, and molten metals. Moreover, *h*-BN exhibits higher oxidation resistance than graphite due to the formation of a dense boron oxide surface layer. Its unique crystal structure provides outstanding thermal shock resistance, easy machinability, and favorable dielectric properties, including a low dielectric constant and low dielectric loss. These characteristics make *h*-BN an ideal candidate for radome fabrication [5–13].

https://doi.org/10.70322/htm.2024.10010

However, the *h*-BN ceramics suffer from inherent low mechanical properties and low oxidation resistance at temperatures above 900 °C [14], which have narrowed the scope of their application. A lot of efforts have been made to enhance the properties of *h*-BN ceramics by adding second phases, such as the fused silica, Al_2O_3, and ZrO_2 [15–17].

Magnesium aluminum silicate is a crucial glass-ceramic system for high-temperature applications due to its high strength (>100 MPa [18]), excellent thermal and chemical stability, low coefficient of thermal expansion (as low as 7 × 10^{-7} K^{-1}, 25~1000 °C [19]) and high melting point (1400–1465 °C). The primary phases of the MAS system include Indialite or α-Cordierite ($Mg_2Al_4Si_5O_{18}$), μ-Cordierite ($Mg_2Al_4Si_5O_{18}$), Mullite ($Al_6Si_2O_{13}$), and Spinel ($MgAl_2O_4$), as well as Mg-Al-Si-O amorphous ceramics. These phases can be changed to the liquid phase at sintering temperature to improve the sintering performance of BN matrix composites [12,20–25]. To date, the mechanical properties, strengthening mechanisms, and thermal shock resistance of MAS-reinforced *h*-BN ceramics have been comprehensively evaluated [8,12,26]. The radomes of hypersonic vehicles are subjected to extreme environments of high heat flow density, rapid warming and chemical erosion, and require materials with ablation-resistant properties at ultra-high temperatures to resist the strong airflow caused by aerodynamic heating during hypersonic flight [27–31]. However, the effect of MAS content on the ablation resistance and ablation surface temperature of the composites is still in a blank stage. The ablation mechanism of BN-MAS ceramic composites with different MAS contents still needs to be investigated.

This study aims to evaluate the ablation performance of BN-MAS ceramic composites using an oxyacetylene torch, with a focus on their potential applications in extreme environments. The effect of MAS content on the ablation behavior was analyzed by examining the ablation mechanism through microstructural observations, surface temperature measurements, phase analysis, and ablation depth distribution. Additionally, the changes in weight and dimensions before and after ablation were investigated to assess the impact of MAS content on the material's degradation.

2. Experimental

BN-MAS ceramic composites with MAS contents ranging from 20~70 wt% were prepared by hot-pressing sintering using BN and MAS powders. MAS powder consists of MgO, Al_2O_3 and SiO_2 mixed according to the stoichiometric ratio of $Mg_2Al_4Si_5O_{18}$. Table 1 provides the detailed compositions of the BN-MAS ceramic composite specimens investigated in this study.

The starting materials were *h*-BN powders (d_{50} = 2.29 μm, purity > 99%, Advanced Technology & Materials Co., Ltd., Beijing, China), MgO (d_{50} = 5.83 μm, purity > 98%, Tianjin Guanfu Fine Chemical Research Institute, Tianjin, China), Al_2O_3 (d_{50} = 0.73 μm, purity > 98%, Showa Denko, Yokohama, Japan), and SiO_2 (d_{50} = 3.39 μm, purity > 98%, Guangyu Quartz Co., Ltd., Lianyungang, China).

The raw powders were combined with Al_2O_3 balls and a sufficient amount of pre-dissolved hydrous ethanol was used as the mixing medium for 24 h. Subsequently, the mixture was dried at 80 °C using a rotary evaporator, and then sieved through a sieve with a pore size of 0.125 mm. The mass ratio of Al_2O_3 balls to powder was 6:1. Finally, composites of 36 mm in diameter and 12 mm in height were prepared by hot-pressing sintering at 1800 °C, 10 MPa pressure, and N_2 atmosphere at 1 atm for 60 min.

Table 1. Compositions of the BN-MAS ceramic composites.

Composites	M20	M30	M40	M50	M60	M70
BN (wt%)	80	70	60	50	40	30
MAS (wt%)	20	30	40	50	60	70

The ablation test was carried out under an oxyacetylene flame in air following GJB323A-96 (China) [32]. The pressures of oxygen and acetylene were 0.4 and 0.095 MPa, while the gas fluxes were 1512 and 1116 L/h, respectively. Heat flux and flame temperature were approximately 4.2 MW/m^2, and 3100 °C, respectively. The ablation specimens (Φ 36 × 10 mm) were fixed into graphite fixtures, and all specimens were polished with sandpaper before the ablation tests. The distance between the nozzle tip and the surface of the specimen was 10 mm, and the flame was perpendicular to the specimen surface. The inner diameter of the nozzle top was 2.0 mm. The surface temperature of the sample was monitored with an infrared thermometer sensor (MODEL: 5R-3015000, IRCON, INC. NILES, IL' MADE IN USA). Before ablation, aim the infrared thermometer sensor at the exact center of the surface of the ablation specimen to accurately measure its surface temperature. The sensor has a temperature measurement range of 800 °C to 3500 °C, with an accuracy of 1% above 1700 °C and 0.5% below 1700 °C. When the flame is stable, the experiment is started and the ablation time is controlled at 15 s.

The phase composition of the samples was identified by X-ray diffractometry (XRD; D/max-γ B, Ricoh, Japan) using Cu-Kα radiation with a scan speed of 4°/min from 10~90°. Microscopic morphology of the samples was characterized by scanning electron microscopy (Quanta 200FEG, FEI, USA; LYRA, TESCAN, CZ). Energy dispersive spectroscopy (EDS) was used to analyze the elemental composition. Confocal microscopy (OLS-3000, Hitachi OLYMPUS, Tokyo, Japan) was used to measure the surface profile of the ablated specimens.

The mass ablation rate and linear ablation rate are calculated by the following formulas [33]:

$$R_m = \frac{m_0 - m_t}{t} \tag{1}$$

$$R_l = \frac{l_0 - l_t}{t} \tag{2}$$

Here, R_m, R_l mean the mass loss rate and linear ablation rate, respectively. m_0 and l_0 mean sample mass and thickness before ablation. m_t and l_t mean sample mass and thickness at the ablation center after ablation, respectively. t means ablation test time.

3. Results

3.1. Ablation Properties and Macroscopical Morphology

Figure 1 illustrates the variation in surface temperature of the composites with different MAS contents. Initially, a sharp increase in the surface temperature of the composites is observed. Subsequently, the temperature stabilizes, reaching a maximum of approximately 2090 °C for samples containing 20 wt% MAS and around 1820 °C for those with 60 wt% MAS. Notably, the surface temperature decreases significantly with increasing MAS content. This represents a marked reduction in ablation surface temperature compared to BN-SiO_2 composites, which exhibit temperatures ranging from 2450 to 2850 °C [10].

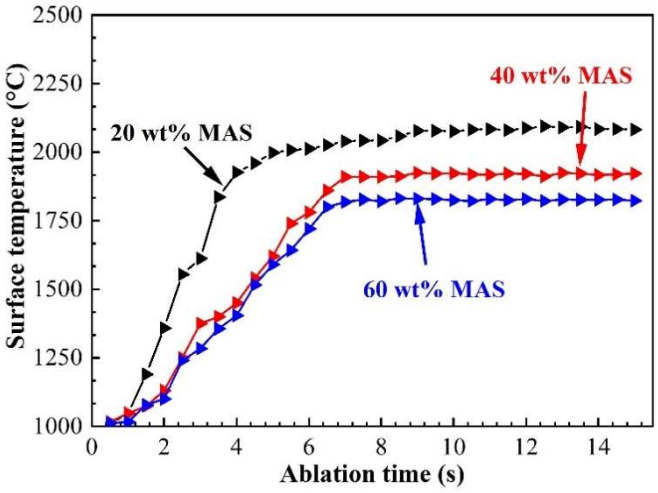

Figure 1. Ablation surface temperature variation of composites with different MAS content.

Ablation properties of BN-MAS ceramic composites are displayed in Figure 2. The results indicate that both the mass ablation rates and linear ablation rates of BN-MAS ceramic composites are correlated with the MAS content. Initially, both the mass ablation rate and the linear ablation rate decrease with increasing MAS content. The composite exhibits optimal ablation resistance at a MAS content of 40 wt%, with mass ablation and linear ablation rates of 0.0176 g/s and 0.112 mm/s, respectively.

Figure 3 presents the macroscopic photographs of the BN-MAS composite surfaces after ablation in an oxyacetylene combustion flame with varying MAS content. Due to thermal stress and gas flow scouring, the surface showed noticeable peeling after the ablation test. Based on the changes in surface morphology, the ablated surface can be divided into three regions, as shown in Figure 3b: the ablation center region (marked as A), the transition region (marked as B), and the heat-affected region (marked as C).

A prominent ablation crater formed in the central region, corresponding to the core area of the flame, with a peak dividing the crater into several sections. Translucent spherical ablation products were observed at the bottom of the crater and in its peripheral areas. When the MAS content exceeded 40 wt%, these spherical products became larger and irregularly shaped. For composites containing 20–60 wt% MAS, no catastrophic damage was observed, even under severe thermal shock conditions, indicating good thermal shock resistance. However, with 70 wt% MAS, cracks began to appear on the surface, suggesting that excessive MAS content weakens the composite's thermal shock resistance.

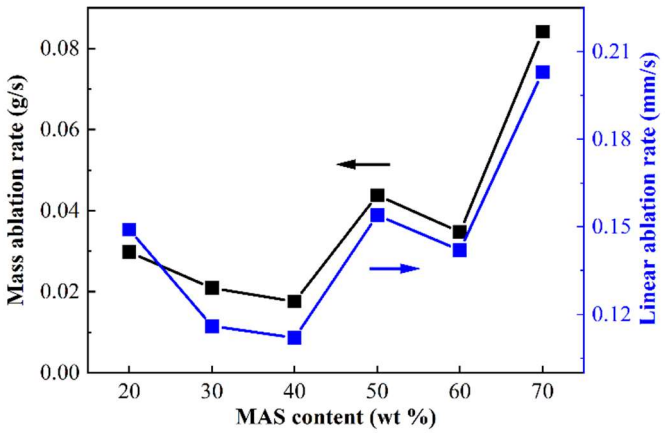

Figure 2. Ablation property of BN-MAS composites.

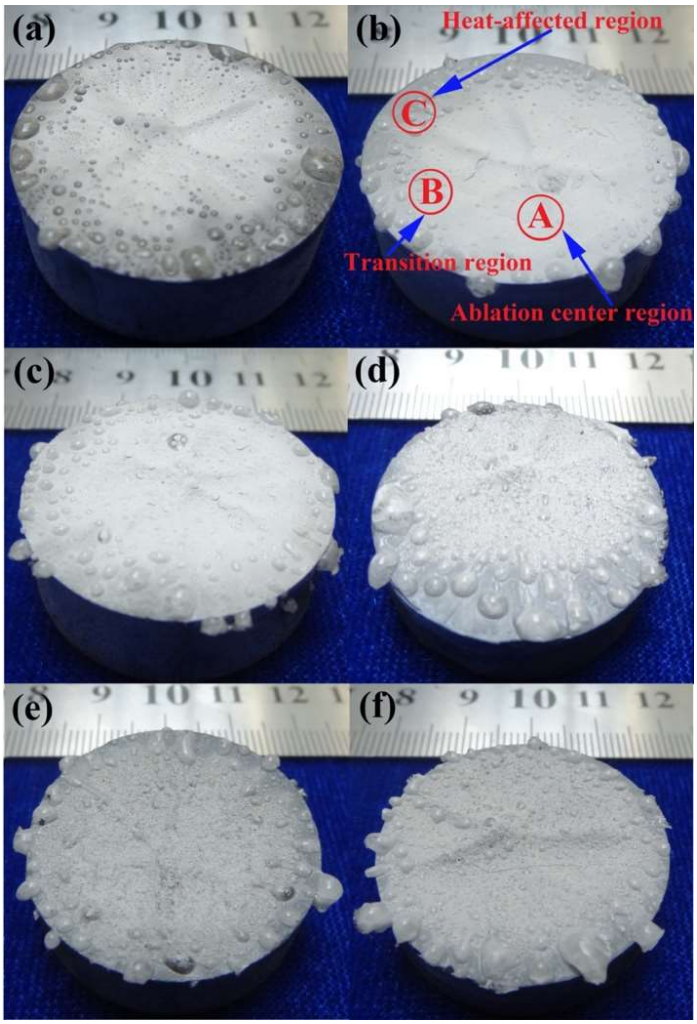

Figure 3. Digital camera images of specimens under different MAS content: (**a**) 20 wt% MAS; (**b**) 30 wt% MAS; (**c**) 40 wt% MAS; (**d**) 50 wt% MAS; (**e**) 60 wt% MAS; (**f**) 70 wt% MAS.

The surface profiles of the central region of each specimen after ablation were characterized using a 3D confocal microscope, as shown in Figure 4. A large number of dense, small burst bubbles and micro-craters were observed on the surface layer of the central region, as illustrated in Figure 4a. As the MAS content increased, the bubbles grew larger, and the surface became more uneven, indicating that the composite suffered significant erosion under such harsh ablation conditions. Additionally, visible microcracks were found in the central region of specimens containing 70 wt% MAS, which can be attributed to the temperature gradient between the ablation center and the edges, promoting crack propagation and pore formation.

On a microscopic scale, the height variation in the ablation center increased with the rise in MAS content, leading to higher surface roughness. This reflects more severe exfoliation, oxidation, melting, and sublimation of the material. When the MAS content exceeded 70 wt%, the matrix became prone to fracture after ablation, indicating a further decline in the structural integrity of the composite under these conditions.

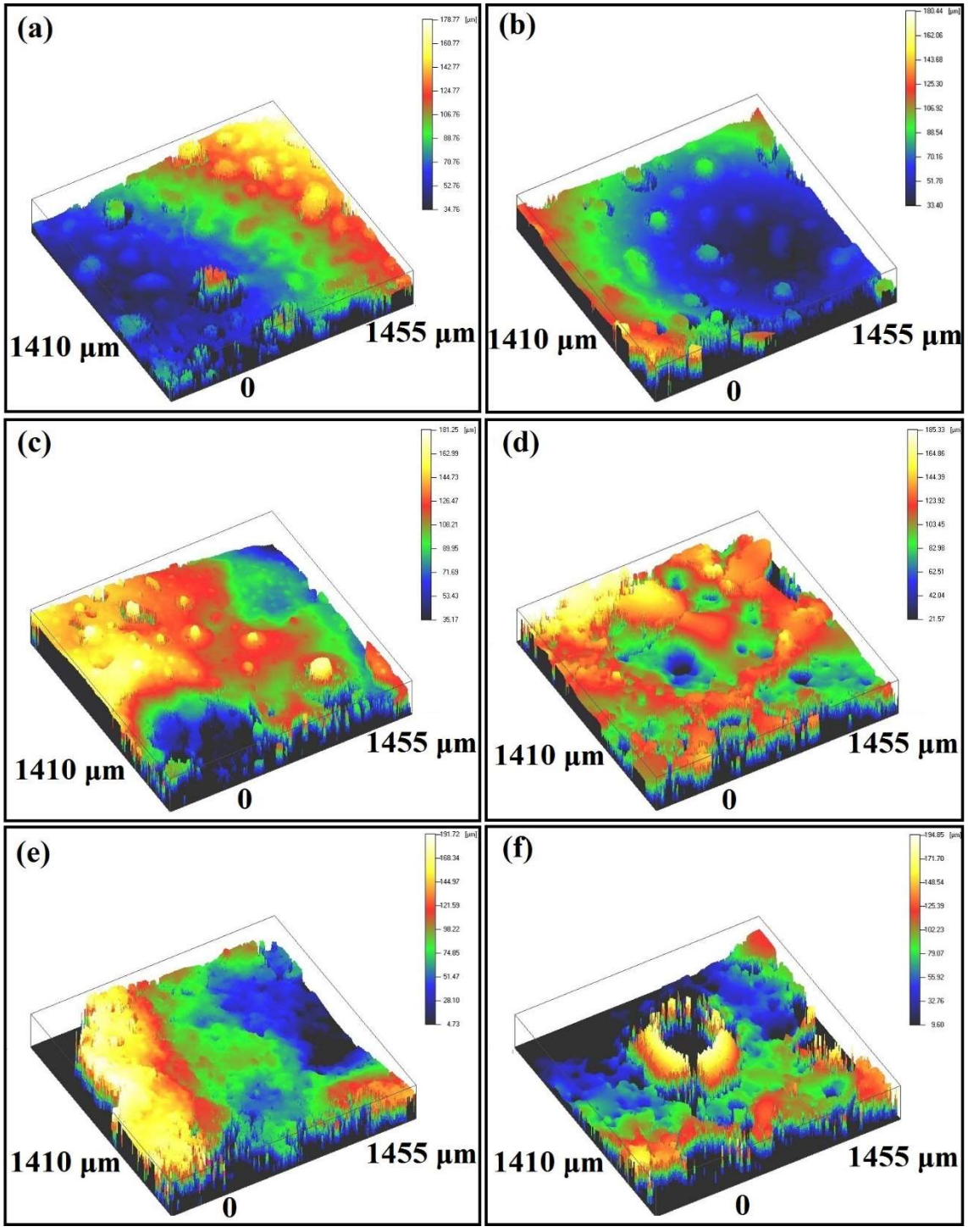

Figure 4. Confocal microscopy images showing the surface profile of specimens after 15 s ablation time. (**a**) 20 wt% MAS; (**b**) 30 wt% MAS; (**c**) 40 wt% MAS; (**d**) 50 wt% MAS; (**e**) 60 wt% MAS; (**f**) 70 wt% MAS.

3.2. Phase Composition and Ablation Morphologies

The XRD of BN-MAS composites containing 50 wt% MAS before and after ablation were analyzed as shown in Figure 5. Before ablation, the composite primarily contained *h*-BN, mullite, and amorphous MAS phase. According to the results of previous studies [8,12,34], BN-MAS ceramic composites were prepared from *h*-BN, MgO, Al_2O_3, and SiO_2 by hot press sintering, and MgO, Al_2O_3, and SiO_2 could form Mg-Al-Si-O glass-ceramics *in-situ* and encapsulate BN particles.

After ablation, the intensity of the mullite phase diffraction peaks decreased compared to that before ablation, and the intensity of the mullite diffraction peaks gradually decreased from the heat-affected region to the ablation central region. New phases did not appear in any region after ablation. Additionally, previous results also studied the effect of MAS content on the phase of BN-MAS ceramic composites [8]. When the MAS content is between 20 and 30 wt%, only *h*-BN peaks are detected, and MAS exists in the form of an amorphous glass phase. When the MAS content reaches 40 wt%, the mullite phase appears, and the amount of mullite formed gradually increases with higher MAS content.

Under ablation conditions, the material was in an oxygen-rich environment, where *h*-BN tended to oxidize to form B_2O_3. B_2O_3 could coalesce with MAS glass to form an amorphous phase, resulting in a higher presence of the amorphous phase on the surface of the sample after ablation. In the ablation transition region and the heat-affected region, the mullite diffraction peaks on the surface were weaker, possibly because the MAS and B_2O_3 coalesced at high temperatures to form a low-viscosity liquid phase, which was blown to the edge of the ablation region by the high-velocity gas flow. As the temperature decreased in the ablation transition region and heat-affected region, the viscosity increased, leaving a large amount of amorphous phase on the matrix surface, which obscured the mullite diffraction peaks. The increase in droplets at the ablation edge can also be seen from Figure 3.

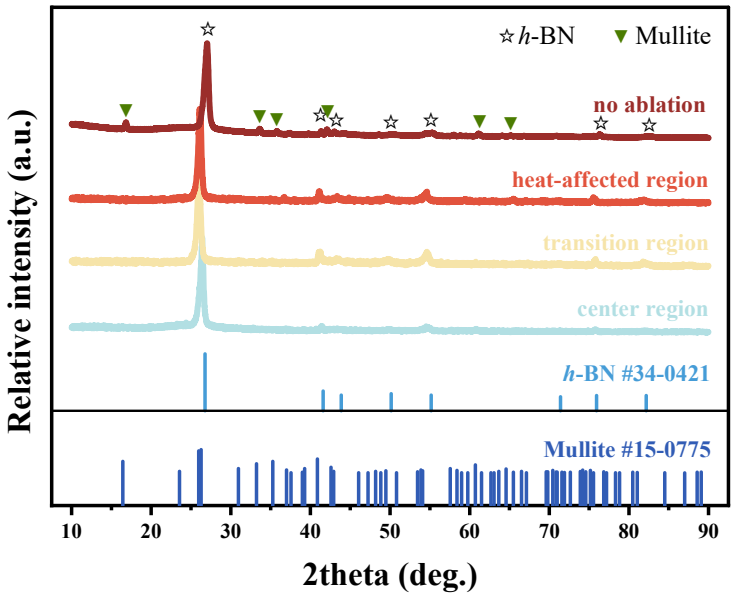

Figure 5. XRD patterns of the surface of BN-MAS composites containing 50 wt% MAS before and after ablation.

Figure 6 shows the original microstructure of the BN-MAS ceramic composite containing 50 wt% MAS, as well as the SEM images of different regions after ablation and the corresponding EDS analyses. Figure 6a shows the microscopic morphology of the surface before ablation. The surface is smooth without obvious macroscopic pores and defects, and has a high relative density.

The ablated composite surface contains both porous and dense morphologies. In the ablation center region and transition region, the sample surface is porous and many platelet particles can be seen. However, the irregular dense phase in the transition region is more than the central region. In the heat-affected region, the sample surface is covered with a dense glass layer with some pores, as shown in Figure 6d. EDS analysis indicates that, in addition to the distinct microstructure differences, there are also significant variations in the elemental composition from the central region to the heat-affected region. The central region and the transition region are rich in Mg and Al elements, whereas the heat-affected region has a higher Si content.

In contrast to the center region, the ablation-flowing gas stream in the transition region is parallel to the surface of the specimen but that is from the nozzle tip to the specimen in the center region. Liquid MAS phase could not only flow

to the adjacent regions from the ablation pits but also evaporation in the center region. Therefore, the transition region is constituted by a thin and relatively dense glassy layer. The analysis of EDS reveals the main components of the surface are Al, Si, Mg, and O elements. With the temperature decreasing from the ablation center to the edge of specimens, the viscosity of the liquid MAS phase also increased. Based on the thermodynamic calculation, the reactions would emit gas phases such as B_2O_3 (*g*), N_2 (*g*), and Mg-Al-Si-O (*g*) during the whole ablation process. Despite the viscosity of liquid MAS increasing, it also could flow on the surface to seal the pores and the ablation surface was covered by a dense SiO_2-rich phase. In addition, some bubbles could be observed from the surface, which were the results of gas emitting and high vapor pressure of magnesium aluminum borosilicate at severe ablation conditions.

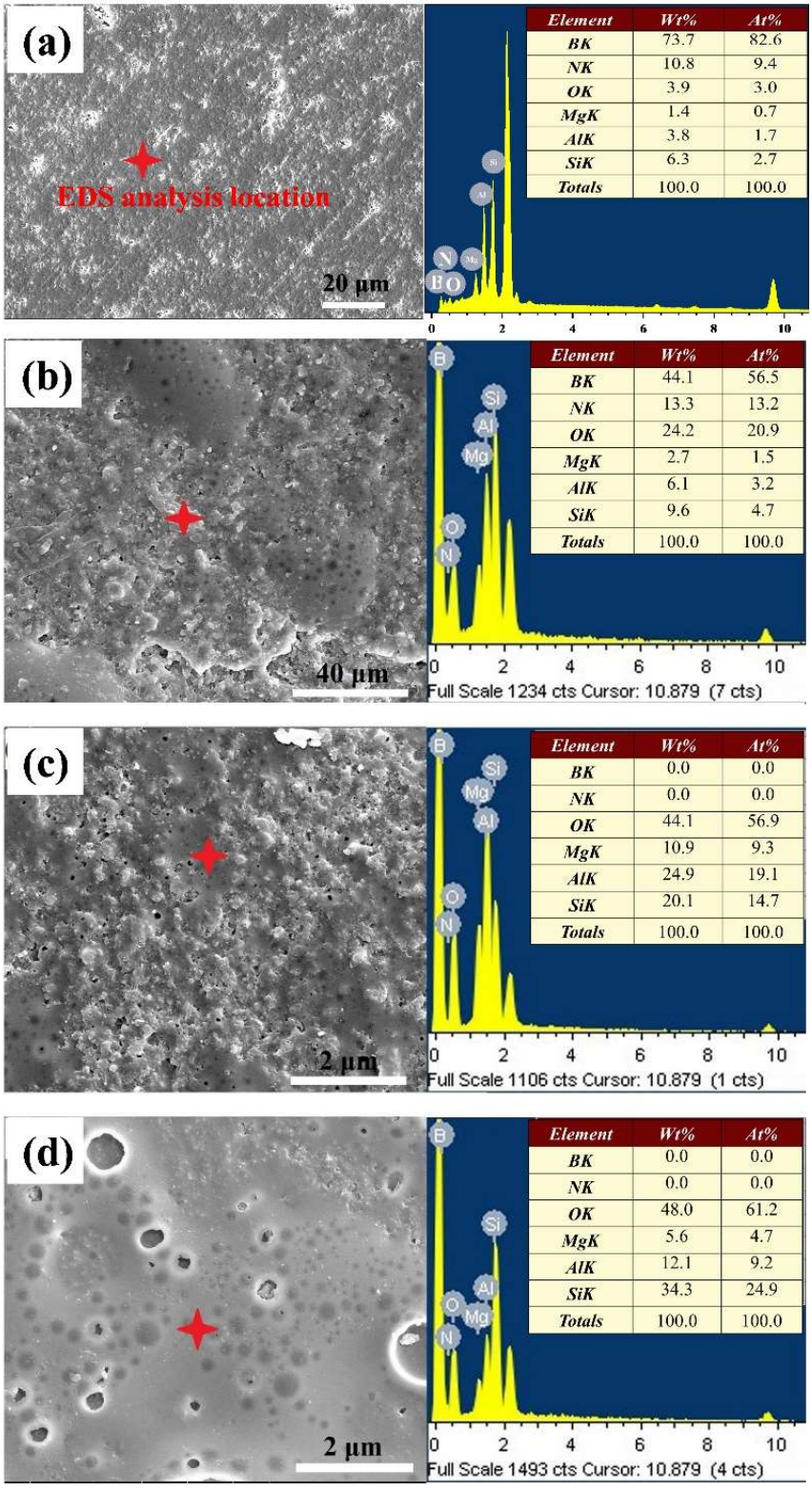

Figure 6. (**a**–**d**) shows the SEM image of BN-MAS composites (50 wt% MAS): (**a**) original surface morphology; (**b**) central region; (**c**) transition region; (**d**) heat-affected region.

The oxyacetylene torch test is highly corrosive, including high temperatures, high-speed airflow, and severe oxidizing environments. The central area of the sample is vertically exposed to the flame; therefore, erosion corrosion is more serious than that in other areas. The cross-section and polishing of the ablation center area provides an in-depth understanding of the microstructure details, which is very noteworthy. Figure 7 shows the microstructure and the corresponding EDS patterns of the ablation center regions of the 30 wt% MAS, 50 wt% MAS, and 70 wt% MAS specimens, which exhibit a distinct oxide layer structure. With the increase of MAS content, the oxide layer thickness gradually increases. The total thickness of the oxidized scale was 1 μm for 30 wt% MAS, 100 μm for 50 wt% MAS, and 300 μm for 70 wt% MAS. The outermost oxide layer of 30 wt% MAS remains relatively dense and continuous. EDS suggests an oxide layer consisting of Mg, Al, Si, B, and O. No obvious transition layer is observed in the center region, indicating the good ablation resistance of the composites. However, numerous microcracks are present in the transition layers of the 50 wt% MAS and 70 wt% MAS specimens. The rapid increase in sample temperature during ablation results in insufficient resistance to the applied aero-thermal load. This temperature surge leads to significant activity of volatile products in the ablation center region, causing micro- and macro-spallation of the sample surface. Once a crack forms, it reduces the overall strength and stiffness of the structure, allowing aggressive agents such as oxygen and high-temperature gases to permeate more rapidly into the matrix, thereby accelerating the degradation of BN-MAS ceramics.

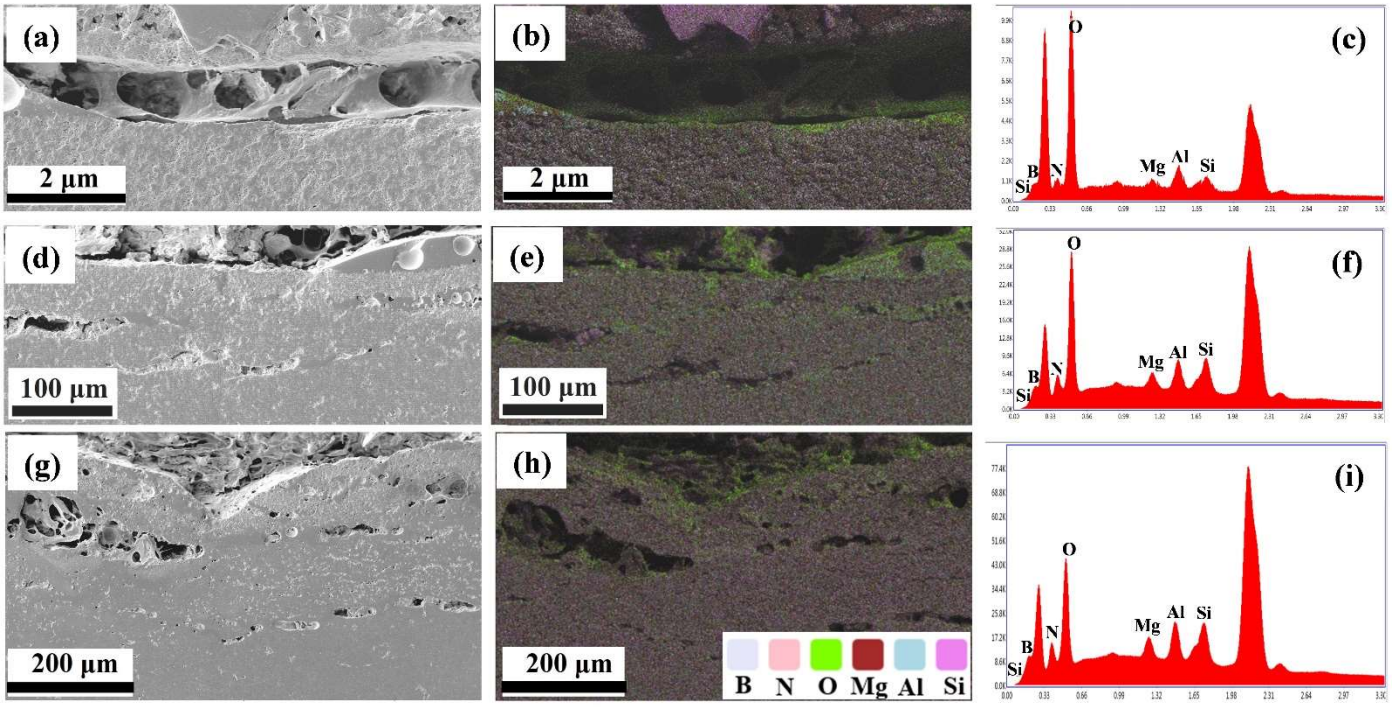

Figure 7. Micro-morphology, elemental distribution and EDS energy spectra of the cross-section of BN-MAS ceramic composites after 15 s ablation. (**a**–**c**) 30 wt% MAS; (**d**–**f**) 50 wt% MAS; (**g**–**i**) 70 wt% MAS.

From Figure 6b, after ablation of BN-MAS ceramic composites, there are a large number of spherical oxidation products. To investigate the structure of the spherical oxidation products and the matrix in the heat-affected region, SEM-EDS analysis of the cross sections is shown in Figure 8. According to the EDS analysis, these particles correspond well with magnesium-aluminum borosilicate glass. In the inner heat-affected region, the BN-MAS composites matrix maintains its own microstructure. The microstructure remained intact and no cracks due to thermal stress were observed. EDS elemental analysis showed no transition layer between the spherical particles and the matrix, which means that oxygen does not penetrate into the BN-MAS composites. The numerous bubbles extant in the particles are caused by gas evolution of B_2O_3 (*g*), N_2 (*g*), and Mg-Al-Si-O (*g*). Most bubbles have not been broken because the viscosity of glass increases gradually during the cooling process. Meanwhile, several microcracks are observed in the spherical particle (Figure 8g), caused by the thermal stress resulting from the mismatch of the thermal expansion coefficients between the magnesium-aluminum borosilicate glass and *h*-BN matrix.

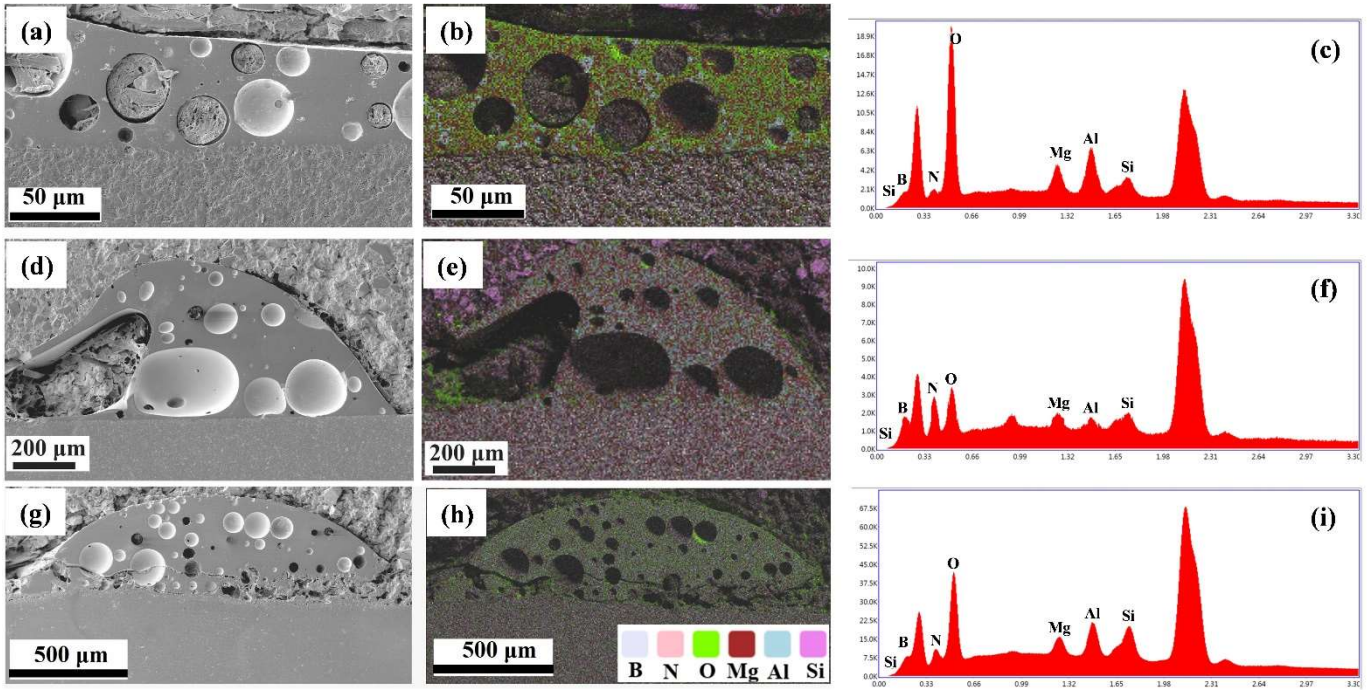

Figure 8. Micro-morphology, elemental distribution and EDS energy spectra of spherical particles in the heat affected region of BN-MAS ceramic composites after ablation. (**a**–**c**) 30 wt% MAS; (**d**–**f**) 50 wt% MAS; (**g**–**i**) 70 wt% MAS.

4. Discussion

4.1. Effect of MAS on Ablation Resistance, Microstructure and Phase Evolution of Ceramic Composites

The observed reduction in surface temperature during the ablation process may be attributed to the partial consumption of heat by the melting and vaporization of MAS, which potentially enhances the high-temperature wave-transmission performance.

The experimental results highlight MAS's critical role in enhancing the ablation resistance of BN-based composites. At an MAS content of 40 wt%, a balance between solid-phase sintering and liquid-phase formation is likely achieved, contributing to the observed improvement in density and reduction in porosity. This may limit oxygen diffusion and reduce the oxidation rate of *h*-BN, leading to a decreased ablation rate.

With varying MAS content, the microstructural evolution appears to influence the ablation performance. Between 20 wt% and 40 wt%, *h*-BN particles are surrounded by amorphous MAS, indicating favorable wettability. As MAS content increases beyond 50 wt%, the mullite phase separates, and weaker bonding regions are observed, potentially decreasing ablation resistance [8]. These trends highlight the need to optimize MAS content to balance the protective effects of the glassy phase while minimizing structural defects.

4.2. Ablation Mechanism

The ablation of BN-MAS ceramic composites under high-temperature oxidizing environments involves both chemical erosion and mechanical spalling, driven by aerodynamic shear forces and thermal gradients. The observed mass loss during ablation is primarily caused by the combined effects of oxidation, sublimation, and material delamination.

Based on the GJB 323A-96 [32], the atmosphere for ablation testing includes 43.02 mol% O_2, 15.38 mol% CO_2, 12.04 mol% CO, and 10.75 mol% O. Thus, the atmosphere used in the ablation experiments of BN-MAS ceramic composites was oxidizing, with an O_2 pressure of 0.43 atm in the ablation atmosphere. During the ablation experiment, the ablation flame temperature is about 3100 °C and surface temperatures of specimens elevate significantly to about 1800~2000 °C detected by the optical pyrometer. Therefore, the oxidation, evaporation and other physical and chemical changes normally take place on composite surfaces. During the oxyacetylene torch ablation, the following reactions might occur:

$$\mathrm{BN}(s)+3/4\mathrm{O_2}(g)\rightarrow 1/2\mathrm{B_2O_3}(l)+\mathrm{N_2}(g) \quad (3)$$

$$\mathrm{B_2O_3}(l)\rightarrow \mathrm{B_2O_3}(g) \quad (4)$$

$$Mg_2Al_4Si_5O_{18}(s) \rightarrow Mg_2Al_4Si_5O_{18}(l) \quad (5)$$

The changes of standard Gibbs free energies and released heats of above reactions between room temperature and 3273 K calculated by HSC Chemistry software were shown in Figure 9. The boiling point of B_2O_3 (*l*) is 1500 °C [14], which is much lower than the ablation flame temperature (~3100 °C). Therefore, under the ablation condition, the reactions above may generate gas emitting and would cause the mass loss of the composites. Meanwhile, the evaporation of B_2O_3 (*g*) and magnesium aluminum silicate (MAS) glass is beneficial to lower the temperature of ablation surfaces, which in turn can improve the thermal protective and wave-transmission performance of BN-MAS composites.

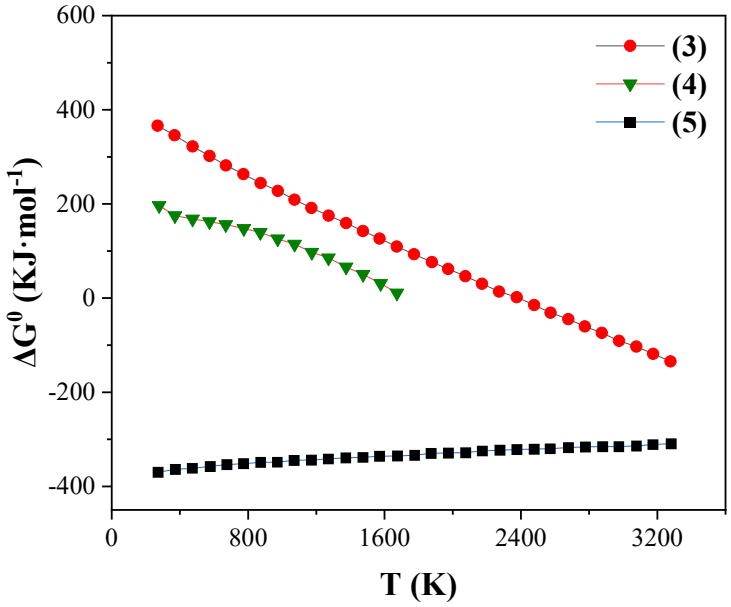

Figure 9. Gibbs free energy of the chemical reactions occurring in the BN-MAS ceramic composites in ablation.

The ablation process likely proceeds in two stages. In the initial stage, the oxidation of *h*-BN leads to porous structures, facilitating gas diffusion and the formation of small pits on the ablation surface. As ablation time increases, B_2O_3 volatilizes rapidly, but its interaction with MAS to form a viscous phase may slow further evaporation and provide limited protection against oxygen ingress [35,36]. At later stages, molten phases volatilize under high airflow, resulting in the loss of protective capacity and the formation of deeper ablation pits.

5. Conclusions

The ablation behavior of BN-MAS ceramic composites was investigated using oxyacetylene torch tests. Surface and cross-sectional analyses were conducted through SEM, EDS, and XRD. Additionally, thermodynamic calculations of selected candidate reactions were performed. The high viscosity of MAS provides effective protection for the BN-MAS ceramic composites against severe ablation from the oxyacetylene torch. Composites containing 40 wt% MAS demonstrate an optimal low ablation rate and a relatively smooth ablation surface, primarily attributed to the self-healing properties of the viscous magnesium aluminosilicate glass.

Author Contributions

D.C. was involved in conceptualization, methodology, data curation and writing—original draft. B.W. carried out article revisions. H.W., B.N., helped get the experimental data. X.L., Y.D., X.W., Z.Y., X.D., D.J., Y.Z. reviewed the article, assisted with resources, and received funding.

Ethics Statement

Not applicable.

Informed Consent Statement

Not applicable.

Funding

This research was funded by the National Natural Science Foundation of China (Nos. 52072088, and 52072089), the Natural Science Foundation of Heilongjiang Province (No. LH2023E061), the Scientific and Technological Innovation leading Talent of Harbin manufacturing (No. 2022CXRCCG001), the Fundamental Research Funds for the Central Universities (No. 3072023CFJ1003), and the National Key Research and Development Program of China (No.2024YFB3714702)

Declaration of Competing Interest

The authors declare that they have no known competing financial interests or personal relationships that could have appeared to influence the work reported in this paper.

Data Availability

The raw data cannot be shared at this time as the data also forms part of an ongoing study.

References

1. Tang S, Deng J, Wang S, Liu W. Fabrication and characterization of C/SiC composites with large thickness, high density and near-stoichiometric matrix by heaterless chemical vapor infiltration. *Mater. Sci. Eng. A Struct. Mater. Prop. Microstruct. Process.* **2007**, *A465*, 290–294.
2. Yang R, Xu J, Guo J, Meng X, Zhang P, Fan F, et al. High wave transmittance and low thermal conductivity Y–*α*-SiAlON porous ceramics for high-temperature radome applications. *J. Adv. Ceram.* **2023**, *12*, 1273–1287. doi:10.26599/JAC.2023.9220756.
3. Feng C, Fang Z, Zhang C. High-temperature properties and associated structure evolution of continuous SiNO fiber-reinforced BN composites for wave transparency. *Mater. Des.* **2013**, *43*, 258–263.
4. Li C, Xia T, Gao S, Yan M, Chen Y, Wan B, et al. Microstructure analysis of quartz fiber reinforced SiO_2 matrix composites by X-ray computed tomography. *Mater. Charact.* **2024**, *209*, 113745. doi:10.1016/j.matchar.2024.113745.
5. Zhang X, Chen J, Zhang J, Wan D, Zhou Y. High-temperature mechanical and thermal properties of h-BN/30vol%Y_2SiO_5 composite. *Ceram. Int.* **2015**, *41*, 10891–10896. doi:10.1016/j.ceramint.2015.05.030.
6. Zhang X, Chen J, Li X, Zhang J, Wan D, Zhou Y. Microstructure and mechanical properties of h-BN/Y_2SiO_5 composites. *Ceram. Int.* **2015**, *41*, 1279–1283. doi:10.1016/j.ceramint.2014.09.058.
7. Eichler J, Lesniak C. Boron nitride (BN) and BN composites for high-temperature applications. *J. Eur. Ceram. Soc.* **2008**, *28*, 1105–1109. doi:10.1016/j.jeurceramsoc.2007.09.005.
8. Cai D, Yang Z, Duan X, Liang B, Li Q, Jia D, et al. A novel BN–MAS system composite ceramics with greatly improved mechanical properties prepared by low temperature hot-pressing. *Mater. Sci. Eng. A* **2015**, *633*, 194–199. doi:10.1016/j.msea.2015.03.030.
9. Cai D, Yang Z, Duan X, He P, Wang S, Yuan J, et al. Inhibiting crystallization mechanism of h-BN on α-cordierite in BN-MAS composites. *J. Eur. Ceram. Soc.* **2016**, *36*, 905–909. doi:10.1016/j.jeurceramsoc.2015.10.007.
10. Wen G, Wu GL, Lei TQ, Zhou Y, Guo ZX. Co-enhanced SiO_2-BN ceramics for high-temperature dielectric applications. *J. Eur. Ceram. Soc.* **2000**, *20*, 1923–1928. doi:10.1016/S0955-2219(00)00107-2.
11. Jia D, Zhou L, Yang Z, Duan X, Zhou Y. Effect of Preforming Process and Starting Fused SiO_2 Particle Size on Microstructure and Mechanical Properties of Pressurelessly Sintered BNp/SiO_2 Ceramic Composites. *J. Am. Ceram. Soc.* **2011**, *94*, 3552–3560. doi:10.1111/j.1551-2916.2011.04540.x.
12. Cai D, Yang Z, Duan X, Zhang Q, Li Q, Li Q, et al. Influence of sintering pressure on the crystallization and mechanical properties of BN-MAS composite ceramics. *J. Mater. Sci.* **2016**, *51*, 2292–2298. doi:10.1007/s10853-015-9531-x.
13. Zhang Z, Duan X, Tian Z, Wang Y, Wang L, Chen L, et al. Texture and anisotropy of hot-pressed h-BN matrix composite ceramics with *in situ* formed YAG. *J. Adv. Ceram.* **2022**, *11*, 532–544. doi:10.1007/s40145-021-0553-3.
14. Jacobson N, Farmer S, Moore A, Sayir H. High-Temperature Oxidation of Boron Nitride: I, Monolithic Boron Nitride. *J. Am. Ceram. Soc.* **1999**, *82*, 393–398. doi:10.1111/j.1551-2916.1999.tb20075.x.
15. Li Y, Qiao G, Jin Z. Machinable Al_2O_3/BN composite ceramics with strong mechanical properties. *Mater. Res. Bull.* **2002**, *37*, 1401–1409. doi:10.1016/S0025-5408(02)00786-9.
16. Duan X, Jia D, Zhou Y, Yang Z, Wang Y, Ren F, et al. Mechanical properties and plasma erosion resistance of BNp/Al_2O_3-SiO_2 composite ceramics. *J. Cent. South Univ.* **2013**, *20*, 1462–1468. doi:10.1007/s11771-013-1635-3.
17. Zhang F, Chen M, Wang H, Shao G, Qi Y, Ma C, et al. Effect of ZrO_2 on sintering behavior and properties of h-BN/ZrO_2 composites by spark plasma sintering. *Ceram. Int.* **2022**, *48*, 34877–34884. doi:10.1016/j.ceramint.2022.08.077.
18. Hu C, Wu J, Xu X, Chen P. Investigating the effect of andalusite on mechanical strength and thermal shock resistance of cordierite-spodumene composite ceramics. *Ceram. Int.* **2018**, *44*, 3240–3247. doi:10.1016/j.ceramint.2017.11.096.

19. Oliveira FAC, Fernandes JC. Mechanical and thermal behaviour of cordierite–zirconia composites. *Ceram. Int.* **2002**, *28*, 79–91. doi:10.1016/S0272-8842(01)00061-X.
20. Hwang S-P, Wu J-M. Effect of Composition on Microstructural Development in $MgO–Al_2O_3–SiO_2$ Glass-Ceramics. *J. Am. Ceram. Soc.* **2001**, *84*, 1108–1112. doi:10.1111/j.1151-2916.2001.tb00797.x.
21. Camerucci MA, Urretavizcaya G, Castro MS, Cavalieri AL. Electrical properties and thermal expansion of cordierite and cordierite-mullite materials. *J. Eur. Ceram. Soc.* **2001**, *21*, 2917–2923. doi:10.1016/S0955-2219(01)00219-9.
22. Zhang L, Ferreira JMF, Olhero S, Courtois L, Zhang T, Maire E, et al. Modeling the mechanical properties of optimally processed cordierite–mullite–alumina ceramic foams by X-ray computed tomography and finite element analysis. *Acta Mater.* **2012**, *60*, 4235–4246. doi:10.1016/j.actamat.2012.04.025.
23. Fotoohi B, Blackburn S. Study of Phase Transformation and Microstructure in Sintering of Mechanically Activated Cordierite Precursors. *J. Am. Ceram. Soc.* **2012**, *95*, 2640–2646. doi:10.1111/j.1551-2916.2012.05254.x.
24. Kaneko K, Honbe N, Matsumoto M, Yasutomi Y, Saitoh T, Takigawa Y. Triple-layered, thick glassy grain boundaries in porous cordierite ceramics. *Acta Mater.* **2002**, *50*, 597–604. doi:10.1016/S1359-6454(01)00346-9.
25. Rohan P, Neufuss K, Matějíček J, Dubský J, Prchlı L, Holzgartner C. Thermal and mechanical properties of cordierite, mullite and steatite produced by plasma spraying. *Ceram. Int.* **2004**, *30*, 597–603. doi:10.1016/j.ceramint.2003.07.004.
26. Cai D, Jia D, Yang Z, Zhu Q, Ocelik V, Vainchtein ID, et al. Effect of magnesium aluminum silicate glass on the thermal shock resistance of BN matrix composite ceramics. *J. Am. Ceram. Soc.* **2017**, *100*, 2669–2678. doi:10.1111/jace.14795.
27. Sciti D, Vinci A, Zoli L, Galizia P, Failla S, Mungiguerra S, et al. Propulsion tests on ultra-high-temperature ceramic matrix composites for reusable rocket nozzles. *J. Adv. Ceram.* **2023**, *12*, 1345–1360. doi:10.26599/JAC.2023.9220759.
28. Yang L, Xiao X, Liu L, Luo J, Jiang K, Han X, et al. Dynamic oxidation mechanism of carbon fiber reinforced SiC matrix composite in high-enthalpy and high-speed plasmas. *J. Adv. Ceram.* **2022**, *11*, 365–377. doi:10.1007/s40145-021-0540-8.
29. Ni D, Cheng Y, Zhang J, Liu J-X, Zou J, Chen B, et al. Advances in ultra-high temperature ceramics, composites, and coatings. *J. Adv. Ceram.* **2022**, *11*, 1–56. doi:10.1007/s40145-021-0550-6.
30. Jastrzębska I, Ludwig M, Śnieżek E, Kalęba A, Drożdż P, Szczerba J. Corrosion study of novel Cr-free alumina-spinel refractory material dedicated to the copper industry. *J. Eur. Ceram. Soc.* **2022**, *42*, 7311–7327. doi:10.1016/j.jeurceramsoc.2022.08.038.
31. Jastrzębska I, Piwowarczyk A, Błachowski A, Mandal S. Influence of PbO/CuO ratio on phase composition, microstructure, melt wettability and recyclability of copper slag. *Ceram. Int.* **2024**, *50*, 23315–23330. doi:10.1016/j.ceramint.2024.04.055.
32. *GJB 323A-96*; Test Methods for Ablation of Ablators. Military Standard of the People's Republic of China-General Armament Department: Beijing, China, 1997.
33. Ye Z, Zeng Y, Xiong X, Wen Q, Lun H. Elucidating the role of preferential oxidation during ablation: Insights on the design and optimization of multicomponent ultra-high temperature ceramics. *J. Adv. Ceram.* **2022**, *11*, 1956–1975. doi:10.1007/s40145-022-0659-2.
34. Wang H, Cai D, Yang Z, Duan X, Wang B, Wang B, et al. Influence of sintering temperature on the crystallization and mechanical properties of BN-MAS composites. *J. Am. Ceram. Soc.* **2022**, *105*, 3590–3600. doi:10.1111/jace.18316.
35. Gogotsi YG, Yaroshenko VP, Porz F. Oxidation resistance of boron carbide-based ceramics. *J. Mater. Sci. Lett.* **1992**, *11*, 308–310.
36. He Y, Guo JM, Zhang GW, Chen XL, Zhang JC, Huang ZL, et al. Preparation of glass-ceramics in the $MgO-Al_2O_3-SiO_2$ system via low-Temperature combustion synthesis technique. *J. Ceram. Sci. Technol.* **2015**, *6*, 201–206.